ARTICLE

Order-disorder transition in nano-rutile TiO_2 anodes: A high capacity low-volume change Li-ion battery material

Received 00th January 20xx,
Accepted 00th January 20xx

DOI: 10.1039/x0xx00000x

Christian Kolle Christensen,[a] Mohammad Aref Hasen Mamakhel,[b] Ananya Renuka Balakrishna,[c]‖Bo Brummerstedt Iversen,[b] Yet-Ming Chiang,[c] Dorthe Bomholdt Ravnsbæk[a,]*

Nano-sized particles of rutile TiO_2 is a promising material for cheap high-capacity anodes for Li-ion batteries. It is well-known that the rutile undergoes an irreversible order-disorder transition upon deep-discharge. Still in the disordered state the Li_xTiO_2 material retains a high reversible ion-storage capacity of >200 mAh/g. Despite the promising properties of the material, the structural transition and evolution during repeated battery operation has so far only been studied by diffraction-based methods, which only provides insight into the part that retains some long-range order. Here, we utilize a combination of *ex situ* and *operando* total scattering with pair distribution function analysis and transmission electron microscopy to investigate the atomic-scale structures of the disordered Li_xTiO_2 forming upon discharge of nano-rutile TiO_2 as well as elucidate the phase behavior in the material during repeated charge-discharge. Our investigation reveals that nano-rutile upon Li-intercalation transforms to a composite of ~5 nm domains of a layered Li_xTiO_2 α-$NaFeO_2$-type structure with ~1 nm Li_xTiO_2 grain boundaries with a Columbite-like structural motif. During repeated charge-discharge cycling, the structure of this composite is retained and stores Li through a complete solid-solution transition with a remarkably small volume change of only 1 vol%.

Introduction

Titanium dioxide is a highly versatile material known to function as photocatalyst,[1,2] photovoltaic,[3] supercapacitor[4] and for photo-electrochemical water splitting.[4,5] Recently, TiO_2 has proven to be a promising alternative to commercial $Li_4Ti_5O_{12}$ and carbon-based anodes for Li-ion batteries,[6–10] due to its low production cost, high capacity and low environmental impact.[11] The theoretical capacity of TiO_2 (335 mAh/g) is excellent in comparison to $Li_4Ti_5O_{12}$ (175 mAh/g) and decent compared to graphite (372 mAh/g). The discharge potential is significantly higher; typically 1.5 to 1.8 V vs. Li compared to <0.5V for graphite. This results in lower energy density of the cells, however higher anode potential reduces risks of Li-plating and electrolyte decomposition at the anode, which enhances cycle life and battery safety especially when operated at high rates.

[a] *Department of Physics, Chemistry and Pharmacy, University of Southern Denmark, Campusvej 55, 5230 Odense M, Denmark.*
[b] *Center for Materials Crystallography, Department of Chemistry and iNANO, Aarhus University, Langelandsgade 140, 8000 Aarhus C, Denmark.*
[c] *Department of Materials Science and Engineering, Massachusetts Institute of Technology, 77 Massachusetts Ave., Cambridge, MA 02139, USA.*

Electronic Supplementary Information (ESI) available: Overview of known ambient-condition TiO2 polymorphs; PDF analysis of as-prepared rutile TiO2 nanoparticles; GITT data, Le bail fits of PXRD data for the chemical lithiated LiTiO2 material; Raman spectra of chemical lithiated LixTiO2 samples; PDF analysis exploring different TiO2 polymorph as local phases; Illustration of close packed stacking sequence of O3-type and O2-type AMO2 structures; PDF analysis of the chemically lithiated sample using O3-type, O2-type and the distorted α-NaFeO2; result of fracture mechanics analysis. See DOI: 10.1039/x0xx00000x

Under ambient conditions, eight TiO_2 polymorphs are currently known: Anatase, Rutile, Brookite, TiO_2-B (bronze), TiO_2-H (hollandite), TiO_2-R (ramsdellite), TiO_2-II (columbite) and TiO_2-III (baddeleyite) (see further details in Table S1, supporting information). The former four have been widely explored as anode materials in Li-ion batteries. Rutile is a natural choice as it is the thermodynamic stable polymorph and the structure contains one-dimensional channels along the *c*-axis (Figure 1A), allowing for Li-insertion and -extraction. Unfortunately, in the bulk form, rutile displays limited storage capacities of <0.1Li per TiO_2 at room temperature,[12,13] and temperatures of ≥120°C are required to achieve reversible Li-ion storage.[14–16] The poor Li-intercalation in bulk rutile has been associated with blocking of the channels parallel to the *c*-axis along which the diffusion coefficient is nine orders of magnitude higher than in the *ab*-plane.[17–19] Fortunately, the Li-ion storage capacity can be significantly improved by utilizing nano-sized rutile particles.[10,20–23] Previous studies suggest that the smaller the particles, the higher the Li-ion storage capacity,[24] e.g. spherical particles of 50 nm diameter intercalates 0.23Li per TiO_2, while nano-rods with a cross-section of 10 nm intercalate 0.85Li,[23] which corresponds to a capacity of 285 mAh/g.

During Li-insertion in nano-sized rutile, several phase transitions have been reported and it appears that there is some variation in the structural evolution depending on particle size and morphology. A monoclinic distorted lithiated rutile, Li_xTiO_2 has been observed with intercalation of up to

~0.5Li per TiO_2 (Figure 1B).[25–27] This phase has been observed both in theoretical and experimental studies.

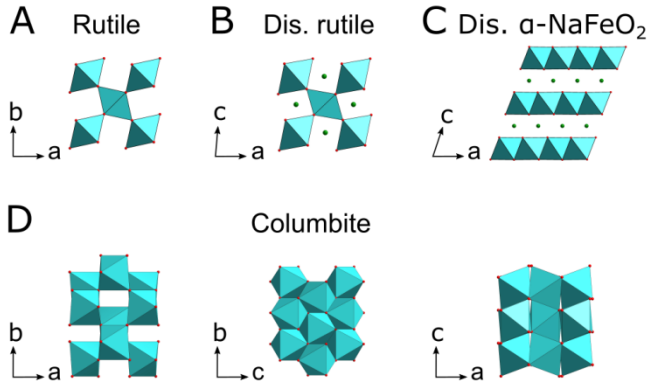

Figure 1. Crystal structures of TiO_2 and Li_xTiO_2 polymorphs relevant in this study: (A) Rutile, (B) monoclinic distorted Rutile, Li_xTiO_2 ($P2/m_{RUT}$), (C) monoclinic distorted α-$NaFeO_2$-type Li_xTiO_2 ($P2/m_{HEX}$) and (D) Columbite, TiO_2-II, viewed along the three unit cell axis. [TiO_6] octahedra are shown as light blue polyhedra and Li as green spheres.

The structure has been described using various space group symmetries, but, based on neutron diffraction, space group *P*2/*m* (often denoted $P2/m_{RUT}$) seems to be a good choice.[25] With Li-insertion beyond ~0.5Li, a two-phase transition is observed. The appearing phase has a low degree of crystallinity and only a few broad Bragg reflections are generally observed.[21,23,25,28,29] This complicates analysis using traditional diffraction methods, which so far have been the main tool in the structural investigations. Diffraction data has however allowed for indexing and several structures have been suggested, i.e. a *Fm*-3*m* rock salt structure, a *R*-3*m* hexagonal[30] structure and a closely related *P*2/*m* monoclinic structure. In the rock salt structure, the cations may be randomly distributed on the octahedral sites in the cubic close packed (ccp) oxygen lattice, while in the latter two structures, the cations are ordered within the ccp oxygen lattice such that alternating Ti- and Li-layers are formed (Figure 1C). The hexagonal structure is an α-$NaFeO_2$-type structure, which also represents other very well-known electrode materials of the $LiMO_2$ family, e.g. $LiCoO_2$ and $Li(Ni,Mn,Co)O_2$ (the so-called NMC).[30] The *P*2/*m* structure is simply a monoclinic distortion of the hexagonal structure and is thus often denoted $P2/m_{HEX}$ not to confuse it with $P2/m_{RUT}$. The $P2/m_{HEX}$ structural model has been confirmed both by powder neutron diffraction and first principle calculations.[25,26]

Hence, previous investigations provide some insight into the evolution of the long-range order structures in nano-rutile during Li-insertion with the assignment of various crystalline phases. However, detailed knowledge is lacking on several levels. Firstly, and most importantly, the transformations beyond insertion of ~0.5Li per TiO_2 results in a significant loss of crystallinity, which simply cannot be explained by crystalline-to-crystalline phase transformation, but must involve amorphization, cracking or nano-crystallization. Secondly, the structural transformations and the underlying mechanism of repeated Li-extraction and -insertion in the disordered Li_xTiO_2 phase remains unexplored. Thirdly, the relation between the observed Li_xTiO_2 polymorphs and the cause of the structural transformations has not been discussed in detail. These questions prompted us to investigate the phase transformation pathway of nano-rutile anodes. To probe both the crystalline and disordered phases in the anode we utilize a combination of powder X-ray diffraction (PXRD), total X-ray scattering (TXS) with pair distribution function (PDF) analysis and transmission electron microscopy (TEM). To achieve insight into the true dynamic transformation pathways, the X-ray scattering experiments were conducted under *operando* conditions. Several recent studies have shown that the structural evolution during battery charge-discharge may differ significantly between static (*ex situ*) and dynamic (*operando*) condition,[31–34] as battery operating conditions inherently are far from equilibrium. Through the combination of these techniques and data refinement, a complete overview of the phase transformations is obtained, and the nature of the disorder induced during discharge is explained. Furthermore, the study reveals the structural phase transformation mechanism during repeated cycling of nano-rutile anodes.

Experimental

Synthesis of TiO_2 rutile nano particles

The synthesis of the TiO_2 rutile nano particles are described in a paper by Mamakhel et al.[35] Herein, 200 mL of 1.6 M HCl solution was kept under magnetic stirring and a mixture of 25 mL Titanium (IV) isopropoxide, $Ti(OC_3H_7)_4$ (97%, Sigma-Aldrich), and 25 mL isopropanol (99.8%, Sigma-Aldrich) was added. Initially a white suspension was obtained, which after heating dissolved to give a clear solution. The transparent solution was heated in a Teflon-lined autoclave at 200°C for 12h and subsequently cooled to room temperature. The resulting titanium dioxide powders were separated in a centrifuge (7000 rpm for 10 min) washed several times with deionized water and ethanol and dried at 105°C overnight in a vacuum oven.

Electrochemical cell assembly and electrochemical characterization.

The as prepared TiO_2 nano particles were mixed in acetone with carbon (SuperP C45) and polyvinylideneflouride (PVDF) in weight ratio 8:1:1 wt% in acetone. The slurry was coated on to a glass plate, left to dry and scraped off to obtain a powdered mixture. The mixture was uniaxial pressed into Ø 6mm free standing pellets of approx. 12 mg. Galvanostatic cycling and galvanostatic intermittent titration (GITT) tests were performed in two electrode Swagelok cells with Li foil as counter electrode and Whatman GF/B separator soaked with seven drops of 1M $LiPF_6$ in ethylene carbonate : dimethyl carbonate 1:1 v/v (99.9%, Solvionic). Galvanostatic cycling was performed in the potential window 1.0 to 3.0 V with a current density of 33.5 mAh/g (C/10) unless otherwise noted.

Chemical lithiation

The TiO_2 nano particle powders were dried 2 days under vacuum at 60°C. Approximately 25mg of the particles were

suspended in anhydrous heptane, and 0.5, 0.8, and 1.0 mole equivalent of n-butyllithium (1.6 M in hexane) was added to the suspensions under magnetic stirring in argon atmosphere. The mixtures were left to react for two days and the remaining liquid was removed. The powders were washed in heptane and twice with acetone and dried to obtain powders ranging from a slightly pale blue color to dark blue almost black.

X-ray diffraction and total scattering.

Powdered samples for ex situ powder X-ray diffraction (PXRD) and total X-ray scattering (TXS) were mounted in polyimide tubes (1.0 mm inner diameter, Cole-Parmer). The ex situ PXRD and TXS data of pristine and chemically lithiated samples were collected at beamline ID-11-B at APS, Argonne, USA with a wavelength of 0.2113Å. For operando SR-PXRD and TXS, the cathode pellets were mounted in AMPIX-type battery cells[36] specially designed for X-ray scattering experiments. The cathode pellets were mounted together with 14 mm discs of Whatman GL/B separators whetted with $LiPF_6$ electrolyte as mentioned above and 12 mm diameter discs of the Li-metal anode. The operando PXRD and TXS were performed at the P02.1 beamline at PETRAIII at DESY, Hamburg, Germany with an X-ray wavelength of 0.2073Å. Scattering patterns were collected using total exposure times of 30 and 240 s per PXRD and TXS pattern, respective. A pattern was collected every ~6 min for PXRD and ~30 min for TXS. Scattering patterns (both at PETRAIII and APS) were collected with a Perkin Elmer (XRD1621) area detector. A CeO_2 standard placed at the cathode pellet position in the AMPIX cell was used for calibration. Diffraction spots originating from the anode metal were masked before azimuthal integration of the raw scattering data using Fit2D software.[37] All patterns (for PXRD and TXS separately) were scaled to compensate for beam intensity fluctuations using the intensity of the primary beam shoulder average over a 2θ or q-range at small angles. Sequential Rietveld refinements were performed with the FullProf software, fitting scale factor, cell parameters and FWHM parameter W. For the Scherrer crystallite size analysis, data for the CeO2 standard was used to correct for instrumental broadening. TXS data was treated using the PDFgetX3 software[38] with a upper Q-range cutoff ($Q_{max\text{-}inst}$) at 21Å^{-1} and 24Å^{-1} for operando and ex situ respectively, r_{poly} value set to 0.9Å to obtain PDFs. The structural models were fitted in real space to the PDF data using the PDFgui software.[39] For fitting operando data, a graphite phase was included to account for uncomplete subtraction of the background carbon signal from the AMPIX cell windows and conductive carbon in the pellet (see Figure S1 in supporting information). The result from fitting ex situ data of the pristine material was used with fixed parameters to fit a graphite phase to the remaining carbon signal in the first scan of the operando data. This procedure is preferred instead of simply subtracting a scaled graphite PDF signal, as it allows for small adjustments of the scale and in-plane cell parameter, a, of the graphite component and thereby also for monitoring that the residual signal stays constant in the sequential fitting.

Electron microscopy

Transmission electron microscopy (TEM) was performed on a JEOL 2010FEG operated with acceleration voltage at 200kV.

Raman spectroscopy

Raman spectra were measured on a Renishaw Invia Reflex Micro Raman using a 532nm 75mW laser operated at 10% power. Spectra of the powders were collected with 1s exposure using a 10x objective.

Fracture analysis

Following Hu et al.,[40] we assume pre-existing crack-like flaws in the rutile electrode particle. During a typical charge/discharge cycle, the particle is stressed from lattice mismatch between the lithiated and delithiated phases. This stressed interface contributes to elastic energy in the particle, which can be reduced by electrode fracture.[41,42] However, fracture is accompanied by the formation of two interfaces that increase the surface energy of the system. Therefore, electrode fracture is suppressed when the energy release rate from crack propagation G is less than the surface energy 2γ. The energy released from crack propagation G is a function of electrode geometry Z, elastic modulus E, mismatch strain ϵ and electrode particle size d. Electrode fracture is suppressed for:

$$G(Z, E, \epsilon, d) < 2\gamma$$

$$d_{crit} = \frac{2\gamma}{ZE\epsilon^2}$$

To determine the critical particle size d_{crit} for rutile electrodes, we model an equiaxed particle of 4 µm × 4 µm × 2 µm size in ABAQUS. The elastic constants of rutile used in the finite element simulations were obtained from Murphy et al.[43] The electrode particle deforms during lithium insertion, and the corresponding anisotropic axial strains used in the calculations were ϵ_{11} = 4:76%; ϵ_{22} = 2:92%; and ϵ_{33} = 1:08%. Further details of the finite element procedure can be found in Ref. [39]. Overall, the calculation estimates the critical particle size for rutile electrodes below which crack propagation is suppressed to be $d \sim$ 20nm.

Results and discussion

The phase pure rutile TiO_2 nanoparticles were prepared by hydrothermal synthesis as described by Mamakhel et al.[35] The as-prepared nanoparticles are elongated with diameter of d = 7-15 nm and length of L = 15-50 nm, which is confirmed by TEM. Analysis of the PDF obtained from TXS data reveals that the structure of the as-prepared rutile is better described using a small monoclinic distortion in space group symmetry $P2/m_{RUT}$ (R_w = 12%) compared to the traditional tetrahedral $P4_2/mnm$ symmetry (R_w = 14%) of rutile (See Figure S2 and Table S2 in supporting information). The monoclinic distortion only causes a slight distortion of the [TiO_6] octahedra as seen from the comparison in Figure 1. Fitting the spherical diameter

of the particles in the PDF provides an estimated size of 10-11 nm.

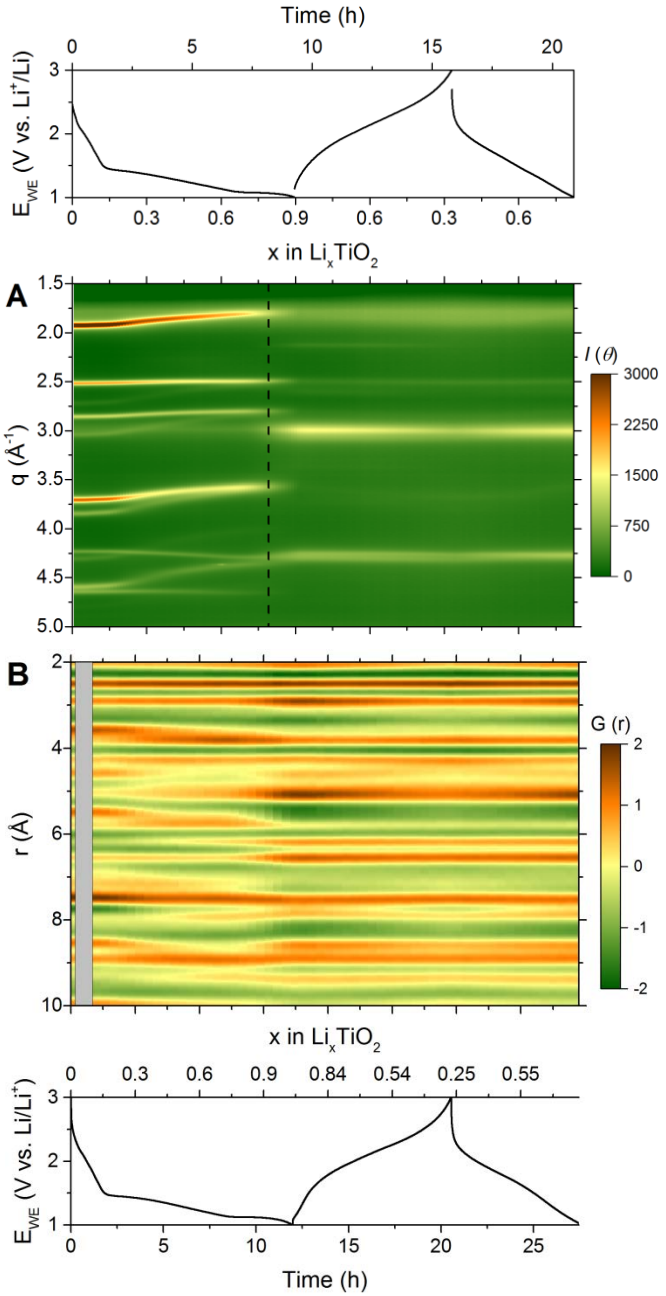

discharge and charge of a nano-rutile TiO2 vs. Li (the grey area in the B correspond to zero intensity due to intermittent loss of the synchrotron beam). The concurrently collected potential profiles are shown above and below the overview plots, respectively.

In the first discharge, the nano-rutile anode takes up ~1Li before reaching the lower potential limit of 1.0 V (Figure 2). In accordance with previous reports the galvanostatic potential profile can be divided into three regimes: Sloping potential up to insertion of ~0.15Li per TiO_2 followed by two plateau-like regions at ~1.4 and ~1.15 V, respectively (see also galvanostatic intermittent titration data in Figure S3, supporting information). From operando PXRD (Figure 2A) it is evident that insertion of the initial ~0.7Li occurs via a solid solution reaction as the Bragg reflections from the rutile structure change angular position continuously and no new peaks appear. The rutile Li_xTiO_2 phase is nicely simulated by Rietveld refinement of the operando PXRD data up to insertion of xLi = 0.78, provided that the monoclinic distorted rutile-like structure ($P2/m_{RUT}$) is used as the structural model in the refinement. The continuous change in lattice parameters during the first Li-insertion is not as pronounced in the PDF overview (Figure 2B) as in the PXRD data, since a small change in lattice parameters is not amplified in the PDFs as in the diffraction case, where $2\theta = 2\sin^{-1}(\lambda/d)$. Still, fitting the PDF data using the same $P2/m_{RUT}$ structural model provides a good fit and nearly identical unit cell parameters. After insertion of 0.78Li, Rietveld refinement of the PXRD data fails as the Bragg peaks of the monoclinic $P2/m_{RUT}$ Li_xTiO_2 become too diffuse. Concurrently, two new peaks appear in the diffraction data at $2\theta \sim 5.5$ and 8° (possibly also at 4° and 5°). Hence, the evolution of the Bragg reflections at the end of the first discharge clearly suggests a two-phase transition between $P2/m_{RUT}$ Li_xTiO_2 and a new disordered or nanocrystalline Li-rich phase with significantly broadened Bragg peaks in comparison to the peaks from the original rutile structure. The crystallite size of the new phase determined by the Scherrer equation (assuming no strain contribution) is ~4.5(5) nm at the end of discharge. The Bragg peaks from the appearing Li-rich phase can be indexed in a cubic *Fm*-3*m* cell (a = 4.1282(4) Å) or two different monoclinic *P*2/*m* cells (a = 5.0144(19) Å, b = 2.88262(5) Å, c = 5.0769(11) Å, β = 72.575(14)° or a = 3.39(3) Å, b = 2.4345(17) Å, c = 2.938(7) Å and β ~ 142.3(4)°). However, evaluating the comparative quality of the models is very difficult (See Figure S4 in supporting information). Hence, we turn our attention to the PDF data.

From the overview plot of the operando PDF (Figure 2B), it is evident that insertion of >0.8Li per TiO_2, causes significant changes in the interatomic correlations, i.e. peaks are disappearing, and new peaks are emerging. This is an evidence of a structural rearrangement. Hence, the monoclinic distorted $P2/m_{RUT}$ rutile-like structure transforms to a new phase with a quite different lattice construction. To characterize the structural details of this phase, a series of three Li_xTiO_2 samples with x ~ 0.5, 0.8 and >1.0 were prepared by chemically lithiation of the rutile TiO_2 nanoparticles using N-butyl-lithium. Ex situ PXRD and PDFs obtained from these samples confirms that at similar degrees of Li-insertion, the same phases are obtained by chemical lithiation as by electrochemical Li-insertion in the operando measurement. The PXRD of the chemically lithiated samples (Figure 3A) confirms that at xLi ~ 0.5, $Li_{0.5}TiO_2$ remains in the monoclinic distorted ($P2/m_{RUT}$) rutile structure, while at xLi ~ 1.0 the sample has completely transformed into the disordered phase showing weaker and broad Bragg reflections corresponding to a crystallite size of 5.0(5) nm based on a Scherrer analysis. At xLi ~ 0.8, both phases are present which confirms the two-phase transition. Raman spectra (Figure S5, supporting information) of the chemically lithiated samples also confirms the drastic loss of crystallinity at higher lithium content, i.e. all Raman shifts loose significant intensity, which is an indicator of

structural disordering. Performing the structural analysis using ex situ rather than operando PDF data, holds the great advantage, that the samples do not contain conductive carbon and binder, which are necessary additives in the functioning

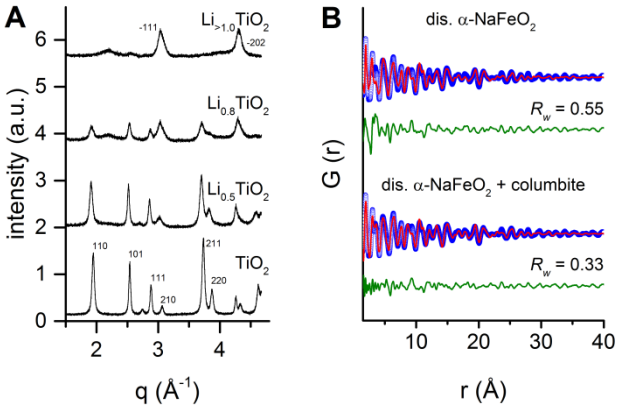

Figure 3. (A) Ex situ PXRD data of pristine TiO_2 nano-rutile and chemical lithiated nano-rutile with compositions $Li_{0.5}TiO_2$, $Li_{0.8}TiO_2$ and $LiTiO_2$. Peak indexes are added for the rutile (bottom) and α-$NaFeO_2$ structures (top), respectively. (B) Fit of the PDF for the chemical lithiated nano-rutile with compostion $LiTiO_2$. The PDF are fitted using (top) distorted $LiTiO_2$ α-$NaFeO_2$–like structure ($P2/m_{HEX}$) and (below) a combination of the distorted $LiTiO_2$ α-$NaFeO_2$–like structure ($P2/m_{HEX}$) and a local LiTiO2 Columbite-like structure with spherical diameter of 9 Å.

electrodes for the operando experiments and unfortunately add to the observed PDF correlations in the lower r-region (r < 5 Å).[44]

In the PDF data (Figure 3B) well defined correlations are observed up to ~50 Å. The medium to long range structure (10 to 40 Å) can be modelled satisfactorily (Figure 3B, top) by a layered monoclinic $LiTiO_2$ structure with space group symmetry $P2/m_{HEX}$ (Table 1 and Figure 1C), as previously suggested from X-ray and neutron diffraction as well as theoretical predictions.[25,26] The spherical domain (or crystallite) size is estimated from the PDF fit to be 51(±17) Å, i.e. ~5 nm. The discrepancy that remains in the PDF fit at higher r (>10 Å) may arise from anisotropic crystallite size. The characterization of the pristine TiO_2 revealed elongated particles, hence it is likely that crystallites of the lithiated phase are also non-spherical.

The structure of the monoclinic $P2/m_{HEX}$ $LiTiO_2$ is a distorted version of the hexagonal α-$NaFeO_2$ prototype structure (spacegroup *R*-3*m*), which is of the rock salt structure family. Thus, the layered $LiTiO_2$ structure consists of ccp layers of oxygen with titanium in half the octahedral holes and Li in the other half. The cations are ordered such that every second layer contains Ti and the others Li. The positions of Li in both rutile and in layered rock salt structures have been subject of several studies of which the majority favors octahedral coordination for Li.[17,18,21,25] Comparing the structures of $P2/m_{RUT}$ rutile-like Li_xTiO_2 structure and the layered $LiTiO_2$ (Figures 1B and C) it is evident that these are linked through a translation along the *c*-axis of the Ti-atoms in every second [TiO_6] layer, i.e. these Ti-atom will move to the layer above and thereby form a denser layer with the [TiO_6] octahedra connected via six edges as opposed to via two edges and six corners in rutile. This may suggest a topotactic transformation. In parallel to the translation of Ti, the oxygen arrangement is changed from hexagonal close packed in rutile to cubic close packed in the layered α-$NaFeO_2$-like structure. This change may be a clue as to why increasing Li-content induces the transformation from a rutile- to an α-$NaFeO_2$-like structure. In rutile, Ti fills half the octahedral holes, and studies suggest that Li will occupy the remaining octahedral positions.[17,18,21,25] Thus, as the Li-content in the Li_xTiO_2 phase increases, the structure will approach a NiAs

Table 1. Structural parameters from fit of the *ex situ* PDF (Figure 3B, bottom) for the chemical lithiated nano-rutile with composition $LiTiO_2$ (corresponding to the fully discharged state) obtained using two phases: The distorted α-$NaFeO_2$–like structure ($P2/m_{HEX}$) and a local Columbite-like structure (fitted parameters are in bold).

Main structure: α-$NaFeO_2$ ($P2/m_{(HEX)}$)			
Scale[a]	**0.263 (±0.065)**	ADPs[b]	
Domain diameter (Å)	**51 (±17)**	Ti U_{iso} (Å^2)	**0.058 (±0.033)**
Quadr. corr. factor	**0.0 (±2.8)**	O U_{iso} (Å^2)	**0.021 (±0.025)**
a (Å)	**5.12 (±0.17)**	α (deg.)	90
b (Å)	**2.902 (±0.081)**	β (deg.)	**69.0 (±1.6)**
c (Å)	**5.10 (±0.12)**	γ (deg.)	90
Atom positions			
	x	y	z
Ti	0	½	½
Ti	½	0	½
O	**0.26 (±0.10)**	0	**0.237 (±0.061)**
O	**0.23 (±0.10)**	½	**0.765 (±0.061)**
Li	0	0	0
Li	½	½	0
Local structure: TiO_2-II columbite			
Scale[a]	**0.737 (±0.065)**	APDs	
Domain diameter (Å)	**8.9 (±1.9)**	Ti U_{iso} (Å^2)	**0.015 (±0.012)**
Quadr. corr. factor	**0.0 (±2.8)**	O U_{iso} (Å^2)	**0.0041 (±0.0062)**
a (Å)	**4.63 (±0.12)**	α (deg.)	90
b (Å)	**4.76 (±0.13)**	β (deg.)	90
c (Å)	**5.42 (±0.11)**	γ (deg.)	90
Atom positions			
	x	y	z
Ti	0	0.1704	¼
O	0.2716	0.3814	0.4142

[a] A global scale factor for the data was fitted to 0.6 (±0.2). The scale of the columbite phase was set to 1 – (scale of α-$NaFeO_2$)

[b] ADP: Atomic Displacement Parameter

structure (hcp of As with all octahedral holes filled by Ni). To the extent of our knowledge, only very few stoichiometric metal oxide adopts the NiAs structure at ambient conditions, e.g. Li_2ReO_3.[45] Thus, as the rutile structure approaches that of NiAs, the continued Li-intercalation forces the structure to change to a rocksalt-like structure type – in this case the layered α-$NaFeO_2$–like structure. This analysis also implies that the composition Li_xTiO_2 is not likely to go beyond *x* = 1Li without a second major structural reconstruction as this would require Li to be intercalated into both the octahedral and tetrahedral holes in the layered Li_xTiO_2 structure.

While the layered α-$NaFeO_2$–like ($P2/m_{HEX}$) Li_xTiO_2 structure explains the PDF correlations at higher *r* (>10 Å), it is evident from the difference plot (Figure 3B, top) that some local structure (*r* < 10 Å) of a highly disordered component is not explained by the layered structure. This is especially pronounced at ~2.0 and 3.5 Å, where the layered structure lacks significant intensity. To investigate the nature of the disordered structure, a long list of TiO_2 and Li_xTiO_2 structures were explored as a second low-order phase. It was easily concluded that tetrahedral [TiO_4] coordination does not form, i.e. no peaks are observed in the PDF between 1.7 to 1.8 Å, where tetrahedral Ti-O distance would be found. In general, Ti is almost exclusively found in octahedral arrangement with oxygen, and rarely in fourfold coordination with a few exceptions (e.g. Ba_2TiO_4).[46] Even in amorphous TiO_2, there are no records of tetrahedral coordination.[47] This suggests that Ti remains in a six-fold coordination. The known TiO_2 polymorphs with [TiO_6]-octahedral coordination represent a wide range of ratios between corners and edges shared per [TiO_6] octahedra (Table 2). Edge sharing octahedra will result in a Ti-Ti nearest neighbour distance of 2.94 – 3.04 Å, while corner sharing octahedra give rise to a broader range of distances of 3.53 – 3.78 Å. The number of correlations in the first and second Ti-Ti coordination shells will naturally depend on the ratios between corners and edges shared per [TiO_6] octahedra. In this context, the layered α-$NaFeO_2$-like ($P2/m_{HEX}$) and Columbite TiO_2 polymorphs constitute the two extremes with ratios of shared corners to shared edges being 0 and 3.5, respectively. Addition of a Columbite-like domain to the fit of the PDF (Figure 3B, bottom), provides a better fit than any other TiO_2 polymorph (Figure S6, supporting information). The Columbite structure is built from 1D zig-zag chains of somewhat distorted edge sharing [TiO_6] octahedra. The chains are connected via corner sharing through seven corners of each octahedra. From the PDF fit, the spherical domain size of the local Columbite structure is estimated to 8.9(±1.9) Å, which corresponds to approximate two Columbite unit cells along all directions. Thus, the Columbite-like domains within the sample should not be regarded as a crystalline Columbite structure but should be considered as small (~1 nm) domains with a structure resembling the Columbite motif with [TiO_6] octahedra sharing in average seven corners and two edges with neighbouring octahedra.

Table 2. Overview of number of edges and corners shared between Ti-O6 octahedra in selected TiO_2 and Li_xTiO_2 polymorphs and their goodness of fit, R_w, when including the polymorph as a local structure with 10 Å spherical diameter as second phase in the fit of the ex situ PDF of $LiTiO_2$ with the distorted α-$NaFeO_2$-like ($P2/m_{HEX}$) $LiTiO_2$ structure as the main phase (see Figure 3B and Figure S6, supporting information).

Structure[a]	Edges shared	Corners Shared	# shared corners / # shared edges	R_w
Columbite	2	7	3.5	0.34
Rutile	2	6	3	0.43
Brookite	3	6	2	0.38
Anatase	4	4	1	0.50
Ramsdelite	4	3	0.75	0.39
Hollandite	4	3	0.75	0.47
TiO2(B)	5	1	0.2	0.47
α-NaFeO2-like	6	0	0	0.56[b]

[a] The Badeleyite structure was also tested. Herein, Ti is coordinated by O in trigonal prismatic geometry. This provided an agreement factor of R_w = 0.44.

[b] The α-$NaFeO_2$-like $LiTiO_2$ is fitted as the global phase (r = 1-14.5 Å). The R_w value is for the fit using only this phase.

We would like to mention, that to validate the interpretation of the PDF analysis other structural scenarios were also explored. Firstly, it was considered if a conversion reaction takes place, i.e. if a reaction between Li and TiO_2 occurs with formation of Li_2O and Ti. The PDF shows no sign of correlations in the low *r*-region typical for Ti and Li_2O,[48,49] and this hypothesis was discarded. Secondly, the option of local disorder due to stacking faults in the layered α-$NaFeO_2$-like Li_xTiO_2 phase was investigated. In the ordered Li_xTiO_2 structure, the cations sit in the octahedral holes in-between the cp oxygen layers, which follow the ccp stacking sequence ABCABC. The cation ordering in alternating layers provides three types of octahedral environments for the cations (between layers A-B, B-C and A-C), hence the structure is denoted an O3-type. Stacking faults would result in a mix between a ccp and hcp lattice, e.g. ABCBABCB. Herein, the cations can be found in two different octahedral sites (between A-B and C-B), hence this structure is denoted O2-type (see also Figure S7, supporting information). An O1-type would have an ABAB O-lattice stacking sequence. This corresponds to a perfect hcp oxygens lattice, which for the composition $LiTiO_2$, where all octahedral holes are filled, represents a NiAs structure. As mentioned, no oxide with this structure type exists to the extent of our knowledge. Thus, the O1-type is omitted in the investigation of stacking faults. To model the degree of stacking faults a mix of the O3-type and O2-type phase were fitted to the PDF in the range r = 1.0 – 14.5Å. However, addition of the O2-phase did not improve the fit (Figure S8 and Table S3), which indicates that no significant amounts of stacking faults are present.

Hence, based on the *ex situ* PDF analysis we conclude that rutile Li_xTiO_2 transforms into a composite of ~5 nm domains of α-$NaFeO_2$-like ($P2/m_{HEX}$) Li_xTiO_2 and ~1 nm highly disordered Columbite-like Li_xTiO_2 domains. This conclusion is cooperated by TEM analysis (Figure 4). Here, we see that the as-prepared rutile TiO_2 and $Li_{0.5}TiO_2$ prepared by chemical lithiation, contains particles of ~10x10x30 nm, which consist of one crystallite, i.e. one coherent atomic lattice extending over the entirety of most particles (Figure 4A). After insertion of ~1Li per TiO_2, TEM reveals that in $LiTiO_2$ the particles contain several smaller crystalline domains of different orientation separated by disordered grain boundaries of 1-2 nm (Figure 4B). The observed TEM intensity within the domains can be

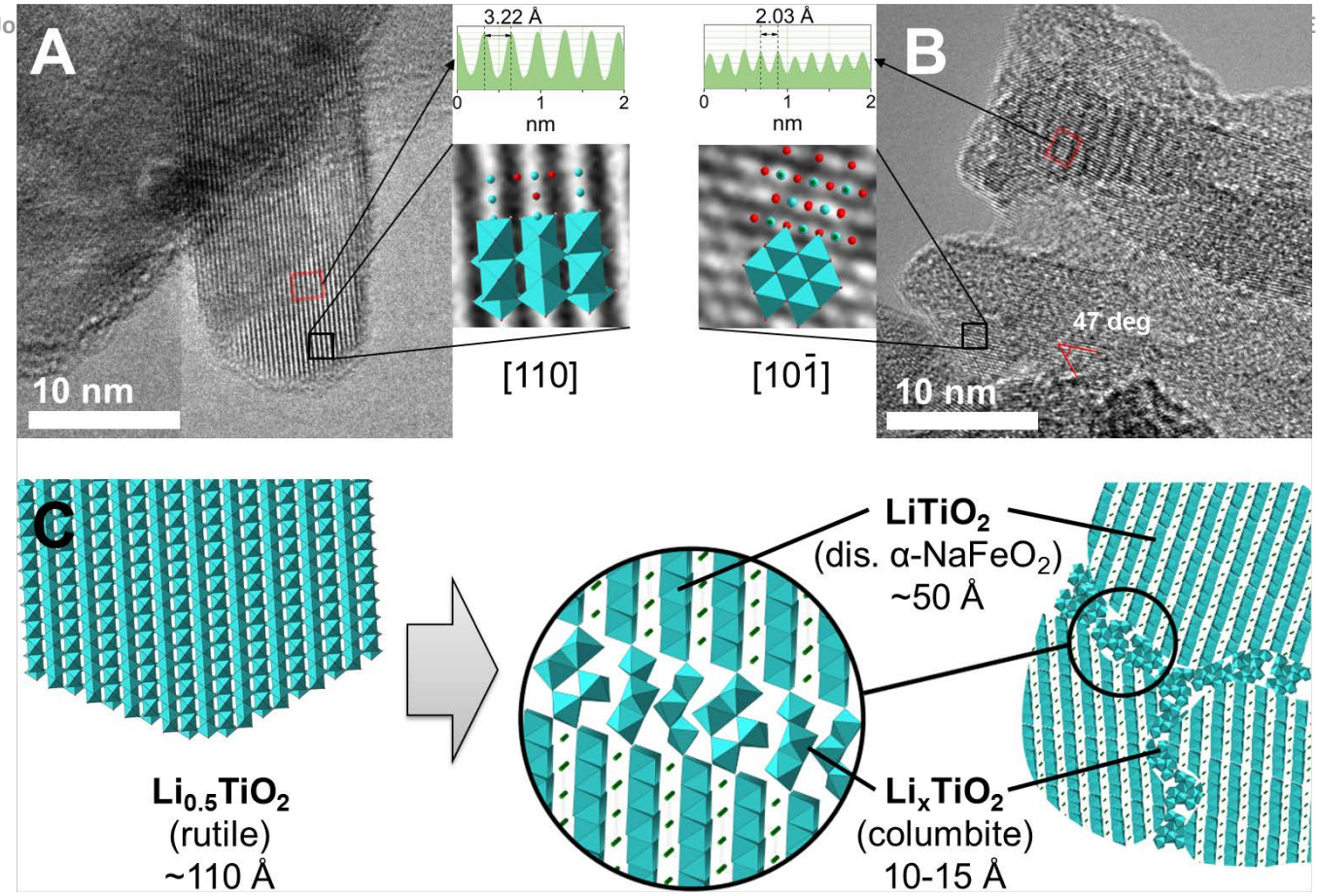

matched with the α-$NaFeO_2$-like ($P2/m_{HEX}$) structure. Hence, based on TEM the columbite-like motifs appear to constitute

Figure 4. TEM micrographs of nano-rutile chemically lithiated to (A) $Li_{0.5}TiO_2$ and (B) $LiTiO_2$, (C) schematic illustration of the structure and local disorder in Li rich nano-TiO_2, showing domains of distorted α-NaFeO2-like structure of ~50 Å size and local disordered regimes best described by a Columbite structure of 10-15 Å, and preserved overall particle size of ~110 Å.

the grain boundaries between the layered $LiTiO_2$ domains. We note that the columbite structure has previously been reported to form as a solid-solid interphase at rutile-anatase grain boundaries.[50] Furthermore, TiO_2 columbite has been shown to be electrochemically active with a capacity of ~70 mAh/g, allowing to reversibly store 0.2 Li per TiO_2.[51] Thus, it is likely that the Columbite grain boundary takes up Li and contributes to the reversible capacity of the electrode. To further corroborate the proposed model, we hypothesized whether the Li_xTiO_2 electrode particles could instead have fractured during discharge. This scenario would imply that the Columbite-like structure forms as a surface layer on the LiTiO2 α-$NaFeO_2$-like ($P2/m_{HEX}$) particles. We test this hypothesis using fracture mechanics.[40] Our analysis estimates the critical particle size below which fracture is suppressed in rutile electrodes to be d ~ 20 nm (see Figure S9 in supporting information). In our experiments, the electrode particles have an estimated size of d ~ 11 nm, which is below this critical particle size. Consequently, we reject the fracture hypothesis in our experiments.

With the knowledge obtained through the ex situ PDF and TEM analysis of the chemical lithiated samples, we can now return to the operando PDF data. Fitting operando PDF of the fully discharged with the α-$NaFeO_2$-like ($P2/m_{HEX}$) – Columbite model obtained from the analysis of the chemically lithiated sample provides a good fit despite the higher noise lievel in the operando data (see Figure S10 in Supporting information). This again confirms the agreement between the structure obtained by chemical and dynamic electrochemical lithiation in this case. Thus, by sequentially fitting the series of operando PDFs using this model, we can understand the dynamic evolution during discharge-charge cycling (Figure 5). During the initial steep potential slope up to ~0.15Li only minor changes occur in the rutile structure. Thus, the current drawn in this regime may not be related to Li-intercalation but originate from formation of e.g. a solid-electrolyte-interface. Between ~0.15 and ~0.8Li, rutile takes up Li via a solid solution reaction, which results in an increasing monoclinic distortion of the unit cell i.e. the a- and b-axis become increasingly different. Note that, the unit cell parameters obtained by PXRD

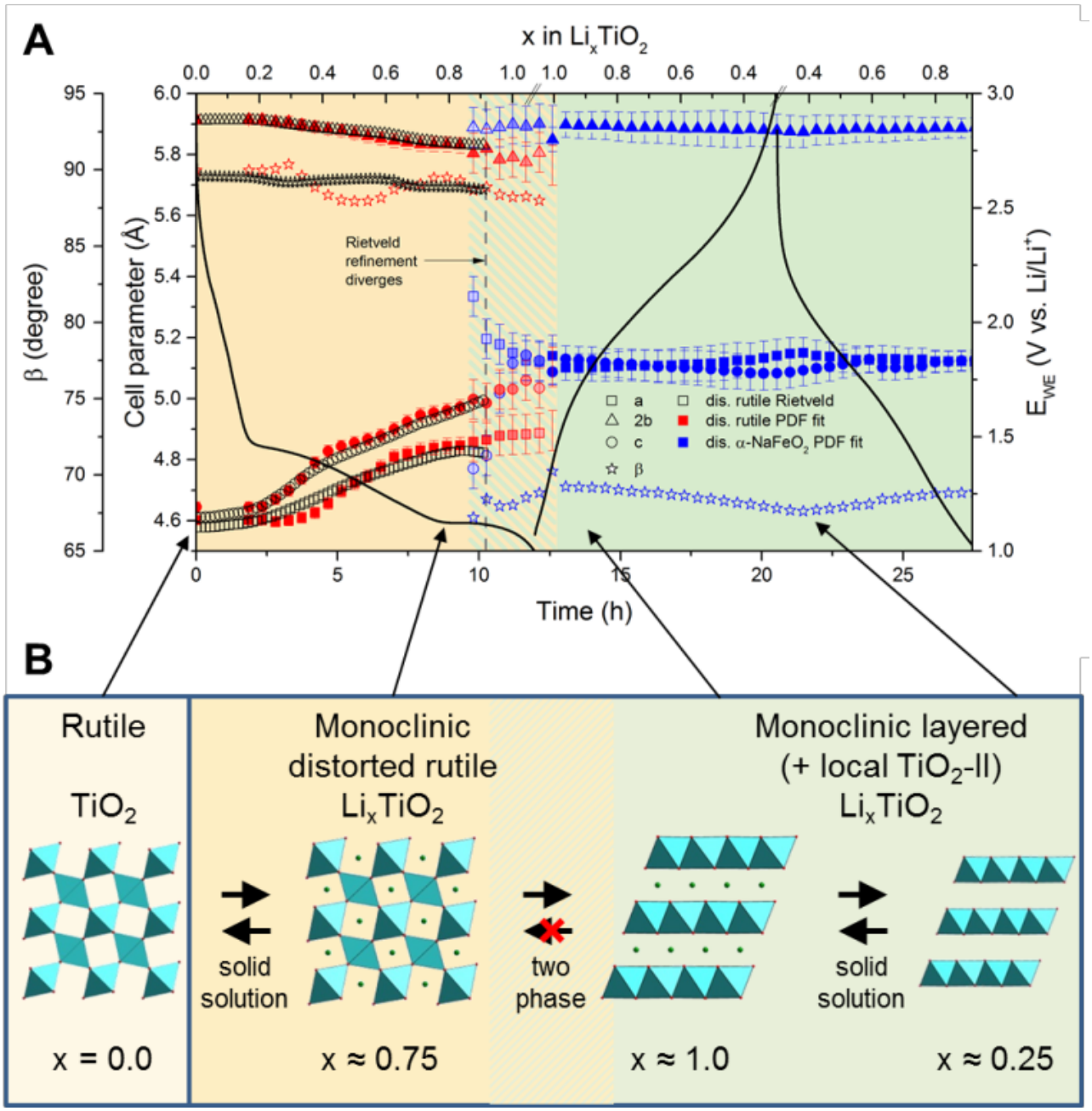

Figure 5. (A) Evolution of the unit cell parameters (*a*, *b*, *c* and β. Note: b-axis plotted as 2*b* for convenience) of the monoclinic distorted rutile Li_xTiO_2 ($P2/m_{RUT}$, empty and red symbols) and layered α-$NaFeO_2$–like Li_xTiO_2 ($P2/m_{HEX}$, blue symbols) structures as a function of Li-insertion and -extraction. The values are extracted by Rietveld refinement of the *operando* PXRD data and by fitting the *operando* PDFs. Note that at the grey dashed line, Rietveld refinement is no longer viable due to loss of diffraction signal. In contrast PDF analysis allows for extracting information about the entire discharge and charge process. The electrochemical data obtained during the TXS experiment is used as representative galvanostatic potential curve (black line). (B) Graphical illustration of the structural transformation at selected points during battery operation (size changes are not to scale).

(Rietveld refinement) and PDF analysis are very similar up to the point (xLi ~ 0.78), where Rietveld refinement fails due to too much disorder. Upon Li-insertion beyond ~0.8Li, the two-phase transition to the layered α-$NaFeO_2$-like Li_xTiO_2 domains with Columbite grain boundaries initiates. The lattice misfit between the monoclinic lattice of the distorted rutile ($P2/m_{RUT}$) and the layered phase ($P2/m_{HEX}$) is very small in this transition, i.e. the misfit between the volume per formula unit is only ~1 % and the linear misfits only ~5, ~1 and ~2 %, along the a-, b- and c-axis, respectively. The layers in the α-$NaFeO_2$-like ($P2/m_{HEX}$) phase are parallel to the *ab*-plane, hence the small linear misfit along the c-axis means that the distorted rutile possibly can transform in a topotactic manner into the layered structure by a translation along the c-axis of half the Ti-atoms. The two-phase transition continues until the Li-content reaches ~1Li per TiO_2 in the electrode. At this

composition the lower voltage limit is reached. During recharge ~0.8Li is extracted while the potential increases continuously without any distinct plateaus. This plateau-less behavior is also confirmed by a galvanostatic intermittent titration (see Figure S3, supporting information). The volume of the layered Li_xTiO_2 decreases continuously during Li-extraction as expected from the decrease in ionic radius of Ti accompanying the oxidation. At the end of charge, the composition of the phase is $Li_{\sim 0.25}TiO_2$ and it is still maintaining the layered α-$NaFeO_2$-like structure and no sign of other phases are observed. Hence, the Li-extraction occurs via a complete solid solution, and it is apparent that the layered material exhibits a wide Li-stability window. At the end of charge, the volume per formula unit of the layered $Li_{0.25}TiO_2$ phase is 35.6 $Å^3$/Z, which corresponds to a volume change of only 1% compared to the fully discharged state. This is significantly smaller than the volume change observed during the first discharge and in general a remarkably small volume change for an intercalation type electrode. Typically, volume changes in intercalation electrodes are 5-10 vol%.[52,53] A small volume change is a tremendous advantage both from a mechanical point of view and in relation to limiting formation of solid-electrolyte-interface (SEI) layers, which is known to shorten battery cycle life. The latter is especially important for the anode. The second discharge follows the same solid solution pathway as observed for the charge and the process appears reversible. Galvanostatic cycling at C/10-rate (Figure 6), shows an initial discharge capacity of 370 mAh/g, which drops to ~220 mAh/g in the second cycle as expected from the operando experiments. Upon repeated cycling, a reversible discharge capacity of >200 mAh/g is maintained for 50 cycles.[54]

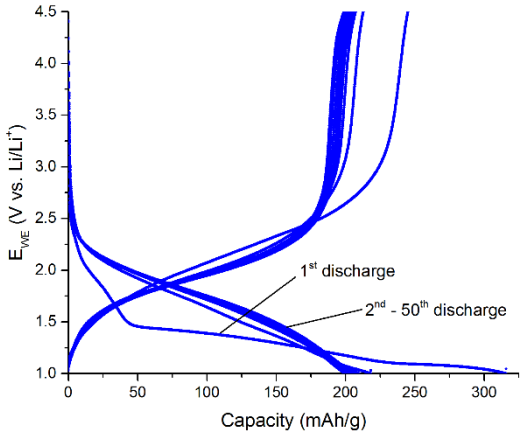

Figure 6. Galvanostatic potential curves for 50 discharge-charge cycles of a 13 nm TiO2 rutile anode vs. Li at C/10 current rate.

Conclusions

The structural evolution during discharge and charge of a nano-rutile TiO_2 anode prepared by hydrothermal synthesis was investigated using a combination of PXRD, TXS with PDF analysis and TEM. The first discharge leads to a monoclinic distortion of the Li_xTiO_2 rutile structure which increases with increasing Li-content. Intercalation of >0.8Li per TiO_2 results in an order-disorder two-phase transition with formation of ~5 nm domains of a layered $LiTiO_2$ α-$NaFeO_2$-like ($P2/m_{HEX}$) phase with disordered grain boundaries, which can be described as ~1 nm domains of Columbite-like Li_xTiO_2. The transformation from the rutile Li_xTiO_2 to the layered $LiTiO_2$ structure may be topotactic and involves a translation of the cations into separate layers and a transition from a hcp to a ccp oxygen lattice. The transition is likely driven by the fact that in a hcp oxygen lattice all octahedral holes cannot be occupied, hence it transforms to a ccp lattice. Upon recharge and subsequent cycling of the battery, the layered Li_xTiO_2 phase stores Li-ion reversibly via a complete solid solution reaction with a remarkably small volume change of just 1 vol% misfit between the completely charged and discharged states. The high reversible capacity of ~200 mAh/g during the 50 tested cycles, the small volume change and the ease of the material synthesis all points to the promise of this disordered anode for Li-ion battery applications.

Conflicts of interest

There are no conflicts to declare.

Acknowledgements

We thank the Villum Foundation (Grant VKR023453), the Independent Research Fund Denmark (Grant 4184-00143A) and the Carlsberg Foundation (Grant CF17-0823) for funding this research. We also thank Danscatt for financial support. BBI and AM gratefully acknowledge support from the Danish National Research Foundation (DNRF93). We are grateful for access to the facilities and resources at the synchrotrons Petra III (beamline P02.1) and the Advanced Photon Source (beamline 11-ID-B). The latter is a U.S. Department of Energy (DOE) Office of Science User Facility operated for the DOE Office of Science by Argonne Nation-al Laboratory (under Contract No. DE-AC02-06CH11357). Finally, we would like to thank Dr. Olaf J. Borkiewicz and Dr. Kamila M. Wiaderek at beamline 11-ID-B (APS), and Dr. Jozef Bednarcik at beamline P02.1 (Petra III) for experimental support.

Notes and references

Abbreviations

ϵ, mismatch strain; γ, surface energy; ADP, atomic displacement parameter; APS, Advanced Photon Source; c, elastic modulus; ccp, cubic close packed; d, particle size; DESY, Deutches Elektronen Synkrotron; E_{WE}, working electrode

potential; *G*, free energy; GITT, galvanostatic intermittent titration technique; hcp, hexagonal close packed; PDF, pair distribution function; PVDF, polyvinylideneflouride; PXRD, powder X-ray diffraction; *Q*, scattering vector; SEI, solid-electrolyte interface; SR, synchrotron radiation; TEM, transmission electron microscopy; TXS, total X-ray scattering; *Z*, electrode geometry.

1 F. Fresno, R. Portela, S. Suárez and J. M. Coronado, *J. Mater. Chem. A*, 2014, **2**, 2863–2884.

2 A. Fujishima, X. Zhang and D. A. Tryk, *Surf. Sci. Rep.*, 2008, **63**, 515–582.

3 A. Kay and M. Grätzel, *Sol. Energy Mater. Sol. Cells*, 1996, **44**, 99–117.

4 B. Chen, J. Hou and K. Lu, *Langmuir*, 2013, **29**, 5911–5919.

5 M. Ni, M. K. H. Leung, D. Y. C. Leung and K. Sumathy, *Renew. Sustain. Energy Rev.*, 2007, **11**, 401–425.

6 T. Fröschl, U. Hörmann, P. Kubiak, G. Kučerová, M. Pfanzelt, C. K. Weiss, R. J. Behm, N. Hüsing, U. Kaiser, K. Landfester and M. Wohlfahrt-Mehrens, *Chem. Soc. Rev.*, 2012, 41, 5313–5360.

7 C. Jiang and J. Zhang, *J. Mater. Sci. Technol.*, 2013, **29**, 97–122.

8 Z. Chen, I. Belharouak, Y. K. Sun and K. Amine, *Adv. Funct. Mater.*, 2013, **23**, 959–969.

9 X. Su, Q. Wu, X. Zhan, J. Wu, S. Wei and Z. Guo, *J. Mater. Sci.*, 2012, **47**, 2519–2534.

10 D. Deng, M. G. Kim, J. Y. Lee and J. Cho, *Energy Environ. Sci.*, 2009, **2**, 818.

11 Z. Yang, D. Choi, S. Kerisit, K. M. Rosso, D. Wang, J. Zhang, G. Graff and J. Liu, *J. Power Sources*, 2009, **192**, 588–598.

12 S. Takai, M. Kamata, S. Fujine, K. Yoneda, K. Kanda and T. Esaka, *Solid State Ionics*, 1999, **123**, 165–172.

13 T. Ohzuku, Z. Takehara and S. Yoshizawa, *Electrochim. Acta*, 1979, **24**, 219–222.

14 L. Kavan, D. Fattakhova and P. Krtil, *J. Electrochem. Soc.*, 1999, **146**, 1375.

15 B. Zachau-Christiansen, K. West, T. Jacobsen and S. Atlung, *Solid State Ionics*, 1988, **28**–**30**, 1176–1182.

16 W. J. Macklin and R. J. Neat, *Solid State Ionics*, 1992, **53**–**56**, 694–700.

17 M. V. Koudriachova, N. M. Harrison and S. W. de Leeuw, *Phys. Rev. Lett.*, 2001, **86**, 1275–1278.

18 M. V. Koudriachova, N. M. Harrison and S. W. De Leeuw, *Solid State Ionics*, 2003, **157**, 35–38.

19 A. Stashans, S. Lunell, R. Bergström, A. Hagfeldt and S.-E. Lindquist, *Phys. Rev. B*, 1996, **53**, 159–170.

20 C. Jiang, I. Honma, T. Kudo and H. Zhou, *Electrochem. Solid-State Lett.*, 2007, **10**, A127.

21 M. Vijayakumar, S. Kerisit, C. Wang, Z. Nie, K. M. Rosso, Z. Yang, G. Graff, J. Liu and J. Hu, *J. Phys. Chem. C*, 2009, **113**, 14567–14574.

22 P. Kubiak, M. Pfanzelt, J. Geserick, U. Hörmann, N. Hüsing, U. Kaiser and M. Wohlfahrt-Mehrens, *J. Power Sources*, 2009, **194**, 1099–1104.

23 E. Baudrin, S. Cassaignon, M. Koelsch, J. P. Jolivet, L. Dupont and J. M. Tarascon, *Electrochem. commun.*, 2007, **9**, 337–342.

24 M. Wagemaker, W. J. H. Borghols and F. M. Mulder, *J. Am. Chem. Soc.*, 2007, **129**, 4323–4327.

25 W. J. H. Borghols, M. Wagemaker, U. Lafont, E. M. Kelder and F. M. Mulder, *Chem. Mater.*, 2008, **20**, 2949–2955.

26 M. V. Koudriachova, N. M. Harrison and S. W. De Leeuw, in *Solid State Ionics*, 2004, vol. 175, pp. 829–834.

27 S. J. Kim, S.-Y. Noh, A. Kargar, D. Wang, G. W. Graham and X. Pan, *Chem. Commun.*, 2014, **50**, 9932–9935.

28 M. A. Reddy, M. S. Kishore, V. Pralong, V. Caignaert, U. V. Varadaraju and B. Raveau, *Electrochem. commun.*, 2006, **8**, 1299–1303.

29 Y. S. Hu, L. Kienle, Y. G. Guo and J. Maier, *Adv. Mater.*, 2006, **18**, 1421–1426.

30 T. A. Hewston and B. L. Chamberland, *J. Phys. Chem. Solids*, 1987, **48**, 97–108.

31 D. B. Ravnsbæk, K. Xiang, W. Xing, O. J. Borkiewicz, K. M. Wiaderek, P. Gionet, K. W. Chapman, P. J. Chupas and Y.-M. Chiang, *Nano Lett.*, 2014, **14**, 1484–1491.

32 K. Xiang, W. Xing, D. B. Ravnsbæk, L. Hong, M. Tang, Z. Li, K. M. Wiaderek, O. J. Borkiewicz, K. W. Chapman, P. J. Chupas and Y. M. Chiang, *Nano Lett.*, 2017, **17**, 1696–1702.

33 D. B. Ravnsbæk, K. Xiang, W. Xing, O. J. Borkiewicz, K. M. Wiaderek, P. Gionet, K. W. Chapman, P. J. Chupas, M. Tang and Y. M. Chiang, *Nano Lett.*, 2016, **16**, 2375–2380.

34 D. R. Sørensen, J. K. Mathiesen and D. B. Ravnsbæk, *J. Power Sources*, 2018, **396**, 437–443.

35 A. Mamakhel, C. Tyrsted, E. D. Bøjesen, P. Hald and B. B. Iversen, *Cryst. Growth Des.*, 2013, **13**, 4730–4734.

36 O. J. Borkiewicz, B. Shyam, K. M. Wiaderek, C. Kurtz, P. J. Chupas and K. W. Chapman, *J. Appl. Crystallogr.*, 2012, **45**, 1261–1269.

37 A. P. Hammersley, S. O. Svensson, M. Hanfland, A. N. Fitch and D. Hausermann, *High Pressure Res.*, 1996, **14**, 235–248.

38 P. Juhás, T. Davis, C. L. Farrow and S. J. L. Billinge, *J. Appl. Crystallogr.*, 2013, **46**, 560–566.

39 C. L. Farrow, P. Juhas, J. W. Liu, D. Bryndin, E. S. Božin, J. Bloch, T. Proffen and S. J. L. Billinge, *J. Phys.: Condens. Matter*, 2007, **19**, 335219.

40 Y. Hu, X. Zhao and Z. Suo, *J. Mater. Res.*, 2010, **25**, 1007–1010.

41 B. Lawn, *Fracture of brittle solids*, Cambridge University Press, Cambridge, 1993.

42 J. R. Rice, *J. Appl. Mech.*, 1968, **35**, 379.

43 S. T. Murphy, P. Zeller, A. Chartier and L. Van Brutzel, *J. Phys. Chem. C*, 2011, **115**, 21874–21881.

44 C. K. Christensen, D. R. Sørensen, J. Hvam and D. B. Ravnsbæk, *Chem. Mater.*, 2019, **31**, 512–520.

45 R. J. Cava, A. Santoro, D. W. Murphy, S. Zahurak and R. S. Roth, *J. Solid State Chem.*, 1982, **42**, 251–262.

46 I. D. Brown and R. D. Shannon, *Acta Crystallogr. Sect. A*, 1973, **29**, 266–282.

47 G. Antonioli, I. Manzini, G. Gnappi and A. Montenero, 1995, **97**, 198–201.

48 T. W. D. Farley, W. Hayes, S. Hull, M. T. Hutchings and M. Vrtis, *J. Phys.: Condens. Matter*, 1991, **3**, 4761.

49 R. A. Patterson, *Phys. Rev.*, 1925, **26**, 56–59.

50 W. N. Zhao, S. C. Zhu, Y. F. Li and Z. P. Liu, *Chem. Sci.*, 2015, **6**, 3483–3494.

51 K. Mukai and I. Yamada, *J. Electrochem. Soc.*, 2017, **164**, A3590–A3594.

52 M. T. McDowell, S. Xia and T. Zhu, *Extrem. Mech. Lett.*, 2016, **9**, 480–494.

53 R. A. Huggins, *Advanced Batteries*, Springer US, Boston, MA, 2009.

54 D. Wang, D. Choi, Z. Yang, V. V Viswanathan, Z. Nie, C. Wang, Y. Song, J. Zhang and J. Liu, *Chem. Mater.*, 2008, 3435–3442.